

## Explosive formation of secondary organic aerosol due to aerosol-fog interactions

Long Jia<sup>a,b,\*</sup>, YongFu Xu<sup>a,b</sup>, MinZheng Duan<sup>c</sup>

<sup>a</sup> State Key Laboratory of Atmospheric Boundary Layer Physics and Atmospheric Chemistry, Institute of Atmospheric Physics, Chinese Academy of Sciences, Beijing 100029, China

<sup>b</sup> Department of Atmospheric Chemistry and Environmental Sciences, College of Earth and Planetary Sciences, University of Chinese Academy of Sciences, Beijing 100049, China

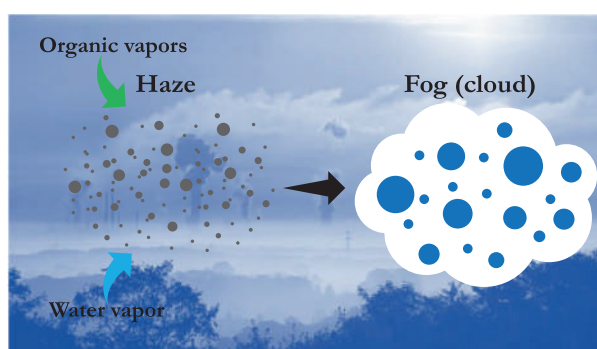
<sup>c</sup> Institute of Atmospheric Physics, Chinese Academy of Sciences, Beijing 100029, China



### HIGHLIGHTS

- Microphysics and chemistry for explosive formation of SOA were studied.
- Organic vapors could lead to the formation of cloud or fog droplets with relative humidity below 100 %.
- Aerosol-fog interactions could result in the explosive growth of SOA.
- Decreasing temperatures could dramatically amplify organic compounds' co-condensing influence on SOA explosive formation.

### GRAPHICAL ABSTRACT



### ARTICLE INFO

Editor: Pingqing Fu

#### Keywords:

Secondary organic aerosol  
Microphysics  
Aerosol-fog interaction  
Explosive growth

### ABSTRACT

Aerosol particles can profoundly affect the local environment and global climate. Explosive growths of secondary organic aerosol (SOA) are frequently observed during serious haze events, but their fundamental mechanism remains unclear. We used chamber experiments and kinetic model simulations to reveal the microphysical mechanism for explosive organic aerosol formation. The evolution of SOA with organic vapors under dry and highly humid conditions was determined based on a high-resolution Orbitrap mass spectrometer. We found that the condensation of gas-phase organics could lead to the formation of cloud or fog droplets with relative humidity below 100 %; meanwhile, the aerosol-fog interaction could result in the explosive growth of SOA. Monomeric products from toluene oxidation were verified to primarily contribute to the increased SOA in super humid conditions, which are mainly assigned to be intermediate- and semi-volatile organic compounds. Moreover, we demonstrated that the decreasing temperatures could dramatically amplify organic compounds' co-condensing influence on SOA explosive formation and activation at relative humidity above 85 % and temperature below 20 °C. Our findings revealed that aerosol-fog interaction is the fundamental driving force for explosive organic aerosol formation. It indicates that overlooking the co-condensation of organic vapors with water could significantly underestimate SOA and liquid water content in 3D models.

### 1. Introduction

Aerosol particles can adversely affect human health and the local environment (Kelly and Fussell, 2015). They can further influence Earth's weather and climate by scattering radiation and acting as cloud condensation nuclei (CCN). Secondary organic aerosol (SOA) is an important fraction of the fine particulate matter (PM<sub>2.5</sub>) in the atmosphere, which is a mixture

\* Corresponding author at: State Key Laboratory of Atmospheric Boundary Layer Physics and Atmospheric Chemistry, Institute of Atmospheric Physics, Chinese Academy of Sciences, Beijing 100029, China.

E-mail address: [jialong@mail.iap.ac.cn](mailto:jialong@mail.iap.ac.cn) (L. Jia).

of organics formed from condensable oxidation products of volatile organic compounds (VOCs). The properties of SOA are closely tied to aerosol-cloud interactions and present the largest uncertainties in estimating the radiative effects for climate change (IPCC 2013).

Fog events were commonly observed during haze days, and a positive correlation between organic aerosol and liquid water content (LWC) was widely detected (Cheng et al., 2021; Fu et al., 2014; Jia et al., 2019; Li et al., 2021; Liu et al., 2021; Quan et al., 2011; Wang et al., 2021, 2020; Yang et al., 2021; Yu et al., 2021). In addition, PM<sub>2.5</sub> explosive growth events frequently occurred during haze-fog periods in China (Guo et al., 2014; Liu et al., 2019; Wang et al., 2018), which were characterized by low temperature and high relative humidity (RH) (Peng et al., 2021). The rapid increase of SOA during serious haze events was mainly attributed to assumptions of aqueous reactions in aerosol water under unfavorable meteorological conditions (Sulaymon et al., 2021; Wang et al., 2021; Zhong et al., 2018). Based on these studies, it can be concluded that the deep interaction of organic composition with aerosol water plays a pivotal role in the explosive formation of organic aerosol. Though China's annual average PM<sub>2.5</sub> has decreased over recent years due to effective emission controls, the abundance of SOA keeps growing and has become the dominant composition of PM<sub>2.5</sub> (Wang et al., 2022). Laboratory measurements show that the contribution of particle water from organic aerosol becomes pretty significant under high humid conditions (Varutbangkul et al., 2006). However, in field studies, LWC was generally predicted by the thermodynamics models (e.g., ISORROPIA or E-AIM) using the inorganic aerosol composition. The role of organic aerosol in the hygroscopic growth of particles was generally neglected due to its complexity. In addition, the shortcomings of these hygroscopicity models are the lack of a coupled consideration of particle curvature (Kelvin effect) and composition (Topping et al., 2005). Since curvature influences the partitioning of volatile compounds between the gas and particle phases, this shortage limits the models' ability to predict the formation of fog or cloud. Hence, though the conversion between haze and fog normally occurs during the haze-fog periods (Yu et al., 2021), the intrinsic relationship between haze and fog is poorly understood.

Unlike nonvolatile inorganic salts, SOA is mainly formed by gas-particle partitioning; thus, the particle-phase concentration of SOA also depends on their corresponding gas-phase precursors. In other words, organic vapors can also affect the hygroscopicity of SOA. The relationship between water vapor and aerosol particles in sub- and super-saturated regimes can be described by the Köhler theory, which combines curvature (Kelvin effect) and solution effect (Raoult's law) (Köhler, 1936). However, classic Köhler theory does not consider the solutes that are soluble gases. Theoretical analysis showed that the presence of HNO<sub>3</sub> or NH<sub>3</sub> vapors could decrease the critical supersaturation point of particles (Hegg, 2000; Kulmala et al., 1997, 1993; Laaksonen et al., 1998), and the presence of organic vapors could enhance cloud droplet number concentrations (Topping et al., 2013). However, these studies are only based on theoretical evaluations, and the direct observational evidence is sparse. The laboratory study by Hu et al. (2018) showed that the presence of propylene glycol vapor could significantly enhance water uptake of ammonium sulfate particles. Since thousands of semi-volatile organic compounds (SVOCs) exist in the atmosphere, SVOCs may affect aerosol hygroscopicity and lead to significant uncertainty for CCN activity (Goulden et al., 2018).

In addition to organic vapors' influence on CCN activation, the condensation of water vapor in SOA formation under super-humid or super-saturated conditions is not well understood. Previous studies mainly focused on the effect of RH on SOA formation under modest humid or sub-saturated conditions, and a positive relationship between RH and SOA yield could be found (Jia and Xu, 2018, 2014; Luo et al., 2019; Wang et al., 2016). Our recent study further found that the increased SOA from toluene oxidation at RH < 90 % was mainly contributed by monomeric products driven by water partitioning (Jia and Xu, 2021). Lamkaddam et al. (2021) found that organics from isoprene could be significantly enhanced on the wetted surface of a flow reactor at RH = 100 %. These studies implied that aerosol water plays a crucial

role in SOA formation. However, since the oxidation of one VOC generally produces hundreds of organics, a typical SOA particle consists of hundreds to thousands of compounds with different structures and vapor pressures (Ziemann and Atkinson, 2012). It indicates that the complexity of SOA-cloud/fog interactions is far beyond inorganics. To the best of our knowledge, no study has been done on direct observation of the evolution of SOA with the influence of organic vapors under super-humid conditions. Thus, to reveal the SOA-fog interaction, a more realistic laboratory study with an online coupling model of explicit chemical reactions and microphysical processes is needed. Benefitting from the most advanced mass spectrometer and an online coupled dynamic model (Jia and Xu, 2021), we can reveal the interaction between haze and fog with the influence of SVOCs from dry to super-humid conditions.

To address these challenges, we investigated the evolution of SOA from toluene oxidation under dry and highly humid conditions through chamber experiments coupled with kinetic model simulations. The changes in SOA molecular composition during the activation process were determined based on an ultrahigh-resolution Orbitrap mass spectrometer. The fundamental role of organic vapors in SOA formation and activation was investigated.

## 2. Methods

### 2.1. Chamber experiments

The experimental schematic setup is shown in Fig. 1. Details of facilities can be found in our previous studies (Jia and Xu, 2021, 2020, 2018; Yu et al., 2022). Here only a brief description is provided. The experiments were conducted at  $20 \pm 1$  °C under low NO<sub>x</sub> conditions with relative humidity at 8 % in a 1.4 m<sup>3</sup> FEP environmental chamber. The UV lights were supplied by UVA-340 lamps (Q-Lab Corporation, USA) with a relative light intensity of 0.20 min<sup>-1</sup> (photolysis rate of NO<sub>2</sub>). Toluene is the precursor of SOA, and the initial concentrations of toluene were 1.3 ppm. The OH radicals were formed from the irradiation of H<sub>2</sub>O<sub>2</sub>. Large diameter Nafion monotubes (Permapure MD-700-48F-3) were used to manage the humidity of the sample air with dry or humid modes. In the dry mode, the shell side of the Nafion tube was purged by dry air (with a dew point of -45 °C), while in the humid mode, the dry air was replaced with deionized water. The RH of the sample air can be controlled to be 8 % RH under the dry mode and 100 % RH under the humid mode, respectively.

The particle concentrations and size distributions in the range of 13–970 nm were determined by a scanning mobility particle sizer (SMPS, Model 3936 TSI, USA), and particles in the size range of 6 nm–10 μm were measured by an electrical low-pressure impactor (ELPI+, Dekati, Finland). To ensure that the equipment temperature was the same as the reactor temperature, we placed the SMPS and ELPI+ inside the enclosure with the reactor. The gas-phase organics were ionized by a modified real-time atmospheric pressure chemical ionization source (APCI) (Jia and Xu, 2021), and the particle-phase organics were ionized by an electrospray ionization (ESI) source. The ions of gas-phase and particle-phase molecular composition were then measured by an ultrahigh-resolution Orbitrap mass spectrometry ( $R = 70,000$  at  $m/z$  200, Q-Exactive Orbitrap mass spectrometer, Thermo Scientific, Germany). After 6 h of reaction, the sample air was introduced into the humid tube (100 % RH), then the sizes and concentrations of SOA were measured by SMPS and ELPI+. Since the flow rate of ELPI+ (10 L/min) is much larger than SMPS (0.2 L/min), a 5 L stainless steel reservoir is connected to the humid tube as a buffer (Fig. 1). The particles from the humid tube were further collected on 25 mm PTFE membranes to determine SOA composition. In addition to sampling through the humid Nafion tube, the sample air was collected simultaneously through a dry Nafion tube to reveal the change of SOA. The SOA particles on the PTFE membranes were extracted with pure methanol and then analyzed by ESI-Orbitrap mass spectrometer. We found that the wall loss of SOA was independent of RH; thus, an average value of  $(3.1 \pm 0.8) \times 10^{-3} \text{ min}^{-1}$  was used in chamber experiments.

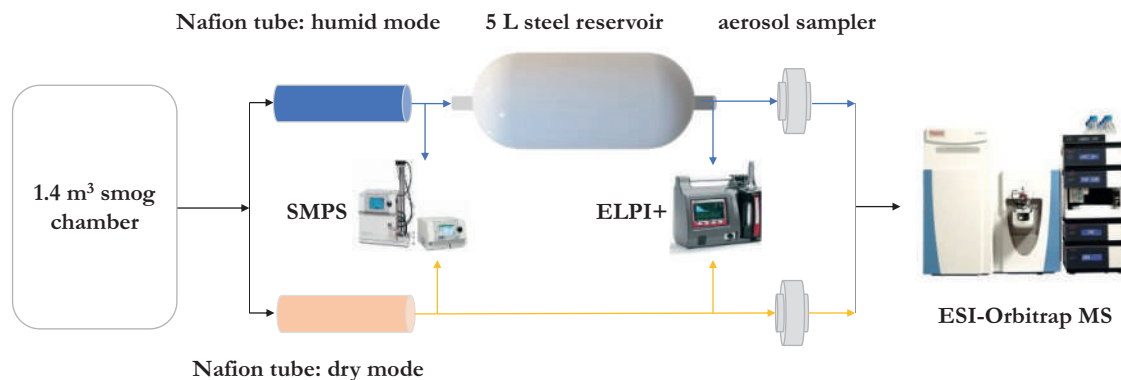


Fig. 1. Schematic diagram of the experimental setup.

## 2.2. Model simulations

A kinetical model of CSVA was used to simulate aerosol-fog interactions. CSVA is a kinetic box model for simulating viscous secondary organic aerosol based on a Core-Shell configuration (Jia and Xu, 2021). In CSVA, the shell part is mainly from low molecular weight monomers, and in the liquid phase, the value of particle-phase diffusion coefficient  $D_b$  is kept a constant shell part. The core-shell structure of SOA will turn into a single liquid state when  $RH > 80\%$ . In the CSVA model, all the processes are represented by “chemical reactions” in a unified form, including gas and particle-phase reactions, homogeneous nucleation, condensation and evaporation (for organics and water). The gas-particle mass transfer is described with the equivalent resistance, which links the gas-phase diffusion, interfacial mass transport and particle-phase diffusion. CSVA can perform kinetic partitioning of water and organics to size-distributed particles, enabling the CSVA to investigate the co-condensation of water and organic vapors before and after the activation of particles. Nevertheless, the original version of CSVA was designed at a given temperature. To expand the application of the CSVA model, we updated the organic particle partitioning equilibrium constant  $K_{pT}$  and surface tension  $\sigma$  to include the influence of temperature on them in this study.  $K_{pT}$  is a function of temperature:

$$K_{pT} = K_{p300} * \frac{T}{300} * \exp\left(1000 * \frac{\Delta H}{R} * \left(\frac{1}{T} - \frac{1}{300}\right)\right) \quad (1)$$

where  $K_{p300}$  is the partitioning equilibrium constant at 300 K, R is the universal gas constant of  $8.314 \text{ (J K}^{-1} \text{ mol}^{-1}\text{)}$ , and  $\Delta H$  is the heat of vaporization ( $\text{kJ mol}^{-1}$ ), which is a function of the organic saturation concentration ( $X^*$ ,  $\mu\text{g/m}^3$ ) determined by a semiempirical equation (Epstein et al., 2010):

$$\Delta H = -11 * \log_{10}(X^*) + 129 \quad (2)$$

The surface tension  $\sigma$  (N/m) depends on  $T$  and solutes (Gysel et al., 2002; Sorjamaa et al., 2004)

$$\sigma = 0.0761 - 1.55 * 10^{-4} * (T - 273) + a X_{salt} + b (1 + X_{salt}) X_{organic} \quad (3)$$

where  $X_{salt}$  and  $X_{organic}$  are the solute molality of salts and organics, and  $a$  and  $b$  are specific coefficients for solutes, with  $a = 3.167 \text{ mN m}^{-1} \text{ L mol}^{-1}$  and  $b = -41.085 \text{ mN m}^{-1} \text{ L mol}^{-1}$  for mixed aqueous solutions of salts and organics. When adapting the effect of temperature on SOA in CSVA, uncertainty may be introduced by the heat of vaporization ( $\Delta H$ ) and surface tension  $\sigma$ . The uncertainty of  $\Delta H$  becomes significant when the  $\Delta H$  is above  $200 \text{ kJ mol}^{-1}$ , as pointed out by Epstein et al. (2010). In our study, the  $\Delta H$  values of primary organics that involve partitioning are in the reasonable range of 48 to  $170 \text{ kJ mol}^{-1}$ . To test the error introduced by  $\Delta H$ , we simulated the SOA with  $(1 \pm 0.05) \Delta H$  under different temperatures and humidity, and the results show that the change of SOA was below  $\pm 4.2\%$ . The simulation results show that the change of  $\sigma$  due to

water-soluble organics had little effect on SOA formation. It agrees well with the previous study that water-soluble organics do not depress surface tension (Ruehl et al., 2016); thus, the effect of water-soluble organics on surface tension can be neglected in this work.

## 2.3. CSVA's ability to simulate the activation of aerosol particles

A detailed description of CSVA's ability to simulate the activation of aerosol particles under super-saturated conditions is presented, which includes some results of the CSVA-predicted Köhler curve for sodium chloride (NaCl) particles and the effect of organic vapor on NaCl activation. Since activation of NaCl particles has been well predicted by the classical Köhler equation (Steinfeld and Pandis, 2016), thus, NaCl particles were chosen to test CSVA's ability to simulate the activation of aerosol particles. Our previous work evaluated the CSVA model and confirmed that CSVA has an excellent performance in simulating size-dependent hygroscopic growth for both inorganic and organics in subsaturated regimes (Jia and Xu, 2021). In this study, we extend CSVA to supersaturation conditions. Here, the activation of NaCl particles with organic vapors is simulated by CSVA. Both hygroscopic growth and activation of salt particles can be described by the Köhler equation, which is the net effect of the Kelvin (the contribution of saturation ratio is always above 1) and Raoult effects (Saturation ratio consistently below 1). Fig. 2 shows the CSVA model predicted Köhler curve of pure NaCl particles at a dry diameter of 50 nm, which shows a maximum (called critical supersaturation ratio,  $S_c$ ) at a critical diameter ( $D_c$ ). The values of  $S_c$  and  $D_c$  from CSVA are consistent with the results predicted by the classical Köhler equation (Steinfeld and Pandis, 2016). It proves that CSVA can simulate the activation of salt particles under super-saturated conditions.

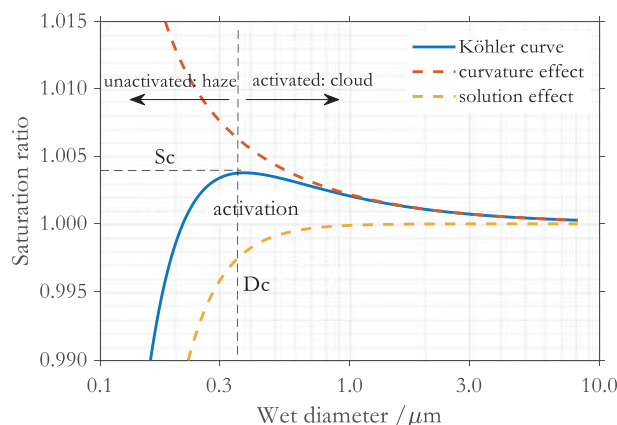
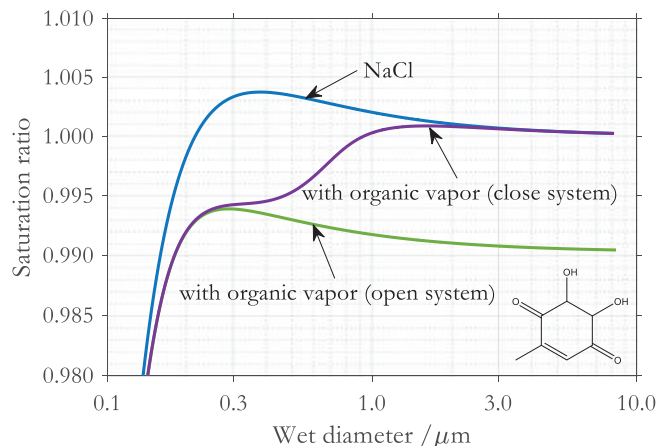


Fig. 2. CSVA predicted Köhler curve for NaCl particles with dry diameters of 50 nm at 293 K.



**Fig. 3.** Equilibrium saturation ratio for NaCl particles without and with semi-volatile organic in the gas phase (PTLQOH, with a gas-particle partitioning equilibrium constant  $K_p = 0.028 \text{ m}^3/\mu\text{g}$ ).

To test the co-condensation of organic vapors with water vapor, we included the partition of a semi-volatile organic compound in the NaCl system. 5,6-dihydroxy-2-methylcyclohex-2-ene-1,4-dione (PTLQOH in MCM, 156 Da) is a typical semi-volatile organic product formed from toluene oxidation in the MCM mechanism; hence PTLQOH is taken as a proxy for SVOCs. The effect of organic vapor on NaCl's activation was simulated in open and closed systems. In the open system, we assume that the sources of organic vapors were so sufficient that the partitioning of vapors to particles did not influence the gas-phase concentration of vapors. Thus, the organic vapor concentration remains constant in the open system and decreases with time due to uptake in the closed system. Fig. 3 shows the co-condensation of PTLQOH and water vapors on NaCl particles with an initial dry diameter of 50 nm. In the open system, the saturation ratio can be reduced due to the addition of solute by continuously partitioning organic vapor, and the Sc value is clearly below 100 % RH (0.994). It shows that the particles can be activated into cloud or fog droplets at RH below 100 % in the presence of organic vapor. In the closed system, the activation experience two stages. In the first stage, the saturation ratio curve is close to that in the open system due to the sufficient PTLQOH in the gas phase; in the second stage, the curve approaches the classical curve due to the depletion of organic vapor from the gas phase. It shows that PTLQOH vapor can significantly reduce the surface water pressure, resulting in a larger particle without activation. The co-condensation effect of water-soluble organic vapors in both open and closed systems is like  $\text{HNO}_3$  vapor (Kokkola et al., 2003; Kulmala et al., 1997, 1993), which confirms the ability of CSVA to simulate the co-condensation of organic vapors during activation.

**Table 1**  
Conditions for the box model simulations.

	Case 1	Case 2	Fig. S4	Fig. S6
MH	600 m	300–1100 m	300–1100 m	600 m
Temperature	273–283 K			
$\text{NH}_4\text{NO}_3$	~	~	~	with
$\text{H}_2\text{O}$ (Southeast wind)	$8.89 \times 10^3$ ppm	$9.57 \times 10^3$ ppm	$7.86 \times 10^3$ ppm	$8.89 \times 10^3$ ppm
$\text{H}_2\text{O}$ (Northwest wind)	$2.74 \times 10^3$ ppm			
Emission rate TOL	$2.5 \times 10^{-2}$ ppm/min			
Emission rate NO	$5.0 \times 10^{-3}$ ppm/min			
Emission rate $\text{NO}_2$	$5.0 \times 10^{-2}$ ppm/min			
Emission rate $\text{SO}_2$	$2.0 \times 10^{-4}$ ppm/min			
Emission rate $\text{NH}_3$	$2.0 \times 10^{-4}$ ppm/min			
Initial $\text{TOL}_{\text{equivalent}}$	0.02 ppm			
Initial NO	0.001 ppm			
Initial $\text{NO}_2$	0.015 ppm			
Initial PM number	500 $\#/\text{cm}^3$			
Initial PM mass	1.0 $\mu\text{g}/\text{m}^3$			

#### 2.4. Simulation of aerosol-fog interaction under ambient conditions

To assess the influence of the aerosol-fog interaction on SOA formation in ambient conditions, we placed CSVA in an Eulerian box skeleton (E-CSVA). The physical framework of E-CSVA includes daily variations of solar radiation, temperature, relative humidity, boundary mixed layer height (MH), dry deposition, wind speed and emissions, which are based on equations from Steinfeld and Pandis (2016). We take Beijing city as an example, and the dimensions for E-CSVA are set to be  $80 \times 80$  km. The weather and environmental conditions are based on the period from 31 October to 7 November 2021. Solar radiation is a function of the zenith angle. The diurnal temperature cycle is based on the model from Göttsche and Olesen (2001), ranging from 0 to 10 °C. The RH is changed with temperature and gas-phase  $\text{H}_2\text{O}$  concentration. MH is based on the observation of Tang et al. (2016), and dry depositions of gases and particles are based on data from Steinfeld and Pandis (2016). The diurnal wind speed patterns are represented by a Gaussian equation referring to the local weather conditions. The velocity of the southeast wind ranges from 0 to 3 m/s, and the northwest wind ranges from 0 to 12 m/s. Toluene is chosen as a base compound for secondary organic aerosol potential (SOAP) evaluation because it is widely recognized as a critical artificial precursor of SOA (Derwent et al., 2010). In E-CSVA, the concentration of  $i$ -th VOC is represented by toluene equivalent concentration ( $\text{TOL}_{\text{equivalent},i}$ ) based on the concept of SOAP, which is described as:

$$\text{TOL}_{\text{equivalent},i} = \frac{\text{SOAP}_i * \text{VOC}_i}{100} \quad (4)$$

where  $\text{SOAP}_i$  is the corresponding SOAP value of the  $i$ -th VOC. Total VOC concentration can be tens to hundreds of ppb in different regions of China (Guo et al., 2017), and aromatics generally account for 20–30 % of total VOCs but contribute the majority of SOAP in Beijing (Li et al., 2020; Sheng et al., 2018; Wei et al., 2018). Based on these studies, the typical total  $\text{TOL}_{\text{equivalent}}$  in the model ranges from 14 to 60 ppb. The detailed conditions for the box model simulations are summarized in Table 1.

### 3. Results and discussion

#### 3.1. Size distributions under different humid conditions

Fig. 4 shows the evolution of SOA mass size distributions in different humid conditions. SOA particles from toluene oxidation mainly display a bimodal size distribution after 6 h of reaction. The mean diameters for the bimodal are 359 nm (the smaller mode) and 615 nm (the larger mode), respectively. The larger mode contributes 87 % of the mass (Fig. 4a). We have demonstrated that the compounds in the larger mode were more volatile than those in the smaller mode, and the bimodal size distribution was mainly attributed to the difference in viscosity caused by

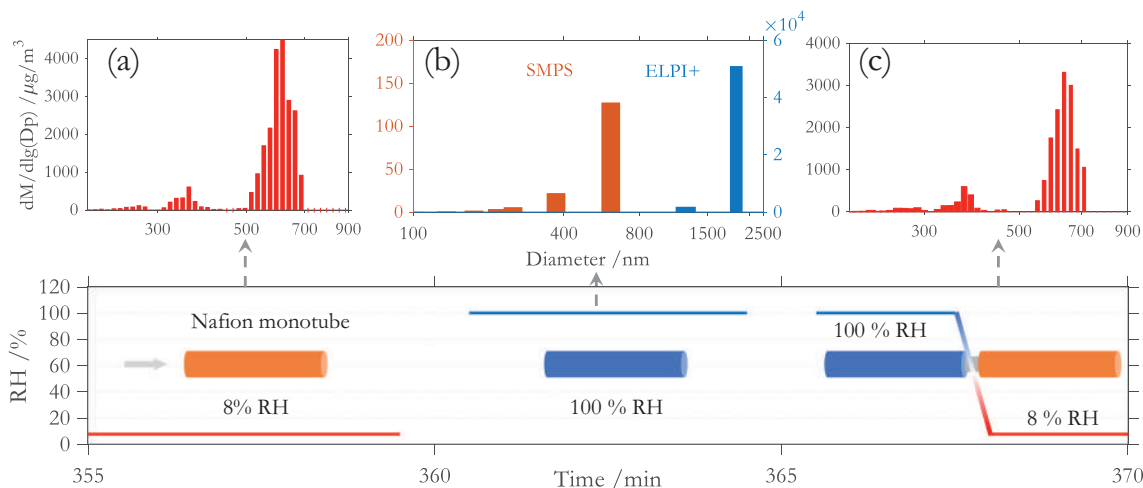


**Fig. 4.** The variations of SOA mass size distribution with different humid conditions through Nafion monotubes: dry mode (a), humid mode (b) and mixing of humid and dry mode (c).

the uneven distribution of oligomers between different modes (Jia and Xu, 2021). When the dry Nafion monotube (RH = 8%) in the sample line of SMPS was replaced with the humid one (RH = 100%), the SOA mass concentration was dramatically reduced from 426.7 to 3.0  $\mu\text{g}/\text{m}^3$  (yellow in Fig. 4b). To confirm that the reduced SOA was not due to the wall loss in the wet tube, we added a dry Nafion tube after the humid one. This setup can help reduce the sample air humidity from 100% to 8%. After such a setup, most particles were observed again (Fig. 4c), indicating that the missing particles did not originate from the wall loss. The reasonable explanation is that the sizes of particles were out of collection range by SMPS due to hygroscopic growth of particles in the humid tube, and that the particles were reduced to the size below one  $\mu\text{m}$  again in the dry tube as a result of dehydration.

To further confirm that the missing particles (by SMPS) were grown or activated into a micron size range in the humid tube, we directly measured the size distribution of particles in the humid tube by an ELPI+ ranging from 6 nm to 10  $\mu\text{m}$ . The ELPI+ results show a clear bimodal size distribution with the mean diameters at 1.32 and 1.96  $\mu\text{m}$  (blue in Fig. 4b). The mass concentration was dominated by the larger size mode at 1.96  $\mu\text{m}$ . The total particle mass concentration was 11  $\text{mg}/\text{m}^3$ , which increased by 27 times compared to the total particle mass at the inlet of the humid

tube. The hygroscopic growth factor (GF) is directly derived from the CSVA model based on the following equation:

$$GF = \sqrt[3]{\frac{SOAV + LWV}{SOAV}} \quad (5)$$

where *SOAV* and *LWV* are volume concentrations of SOA and liquid water. The CSVA model further shows that GF can be as large as 6.5 (100%RH) when considering the uptake of organic vapors. If the co-condensation of organic vapors were excluded, the GF would be <2.7 (at 100% RH) based on the CSVA model. This value also agrees with the SOA GF from  $\alpha$ -pinene and limonene, which was predicted by a thermodynamic model without considering the influence of organic vapors (Liu et al., 2018). If GF were 2.7, the total mass concentration of particles would be <3  $\text{mg}/\text{m}^3$ , which is much less than the observed value of 11  $\text{mg}/\text{m}^3$ .

### 3.2. Molecular composition of increased SOA under super-humid condition

To determine the changes in SOA molecular composition in the humid tube, we simultaneously sampled the SOA through two Nafion tubes in the dry (8%RH) and humid modes (100%RH) for 30 min. The SOA mass spectra from the dry and humid modes are shown in Fig. 5. It shows that the difference in the humid condition causes a visible increase in overall ion abundances. Based on the chromatogram data (not shown), the SOA mass in the humid channel is increased by 67% compared to the dry channel. Based on SOA mass spectra, 77% of increased SOA molecules in the

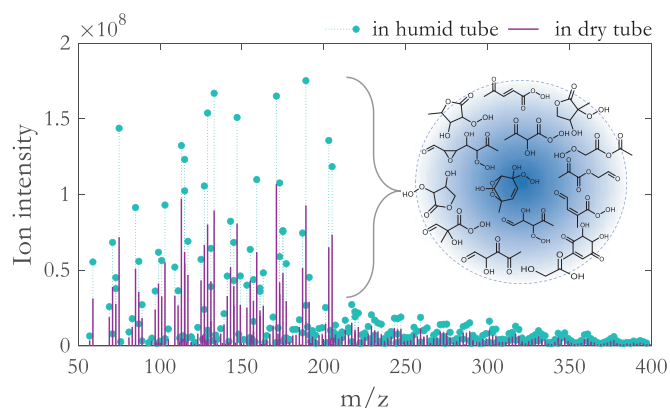


**Fig. 5.** Mass spectra of SOA from toluene oxidations collected through the dry tube pathway (purple) and the humid tube (green). The increased SOA mass concentration was mainly from the uptake of gas-phase monomers (< 210 Da) yielded by gas-phase reactions and oligomers (> 210 Da) formed in particle-phase reactions. (For interpretation of the references to color in this figure legend, the reader is referred to the web version of this article.)

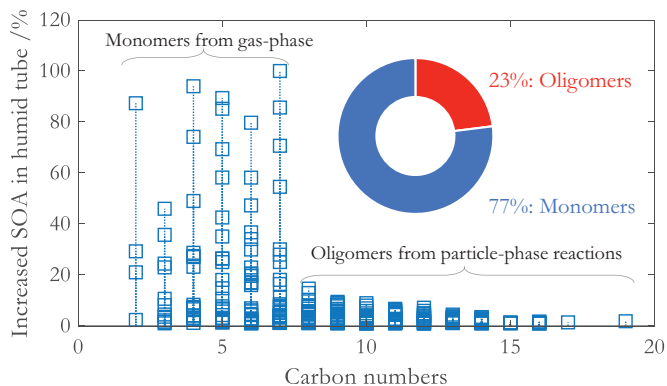


**Fig. 6.** Differences in MS peak abundances between the humid and dry tubes as a function of carbon atoms (Square symbols represent SOA species).

humid tube have an  $m/z$  below 210 Da (Fig. 5). There are 115 molecules identified based on high-resolution mass spectra (Table S1); some representative species are also shown in Fig. 5. It shows that these pieces are mainly monomers that formed from gas-phase oxidation of toluene. In contrast, the ions larger than 210 Da are mainly oligomers formed by particle-phase reactions, contributing to the remaining 23 % of the increased SOA mass.

To trace the formation pathways of increased molecules in the humid tube, we grouped them according to carbon atoms ( $n_C$ ). Fig. 6 shows that the increased species mainly have carbon atoms  $n_C \leq 7$ . Since toluene is a C7 compound, species with  $n_C \leq 7$  are primarily produced by gas-phase oxidation, and the molecules with  $n_C > 7$  can only come from oligomerization. The increased oligomers were below 20 %, while the abundances of some monomers were even doubled in the humid tube. It further supports that those oligomers play a relatively minor role than monomers from gas-particle partition.

Organic species with a high surface affinity can reduce surface tension and further influence the activation process (Davies et al., 2019; Lowe et al., 2019; Ruehl et al., 2016). The O/C ratios can be calculated by the molecular formulas and corresponding abundances. The molecular formulas and corresponding intensities were determined based on high-resolution mass spectra are shown in Table S1. As shown in Fig. S1, the O/C ratios of the uptake species are close to 0.8, indicating that these species are polar and water-soluble. We also did control experiments to test the water solubility of toluene-derived SOA. The SOA particles collected on the ZnSe disk could be fully extracted by one drop of water. Liu et al. also showed that toluene SOA did not form a liquid-liquid phase separation state at high RH due to high water solubility (Liu et al., 2018). Since water-soluble organics do not depress surface tension (Ruehl et al., 2016), the abundance of organics on surface tension can be neglected. Thus, our experimental results provide direct evidence that the increased SOA species in the humid tube result from gas-particle partitioning, which is driven by the condensation of water.

To characterize the volatility, we group the increased compounds in the humid tube into different sorts based on their saturation concentrations,  $C^0$ , in the form of  $\log_{10}C^0$ , here  $\log_{10}C^0$  is predicted based on the equation (Donahue et al., 2011):

$$\log_{10}C^0 = 0.475 \times (25 - n_C) - 1.75 \times n_O \quad (6)$$

where  $n_C$  and  $n_O$  are the numbers of C and O atoms. The volatility distribution of increased species is shown in Fig. 7. It shows that the volatility ( $\log_{10}C^0$ ) decreases with increasing  $n_C$ . The volatility of monomers ranges from  $10^6$  to  $10^{-5} \mu\text{g}/\text{m}^3$ , belonging to IVOC, SVOC and LVOC. In particular, the majority of monomers are IVOCs and SVOCs. In comparison, the volatility of oligomers are mainly LVOCs and ELVOCs. Thus, the MS spectra verify

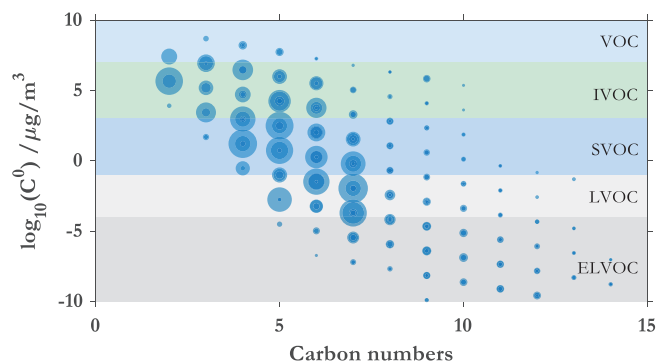


**Fig. 7.** Volatility ( $\log_{10}C^0$ ) is indicated by the saturation concentration  $C^0$  as a function of carbon numbers. VOC, volatile organic compounds; IVOC, intermediate-volatility organic compound; SVOC, semi-volatile organic compound; LVOC, low-volatility organic compound; ELVOC, extremely low-volatility organic compound. Since there may be different molecules with the same carbon atom number, thus, different color shading was used to represent molecules, and the circle size represents the abundance of one species.

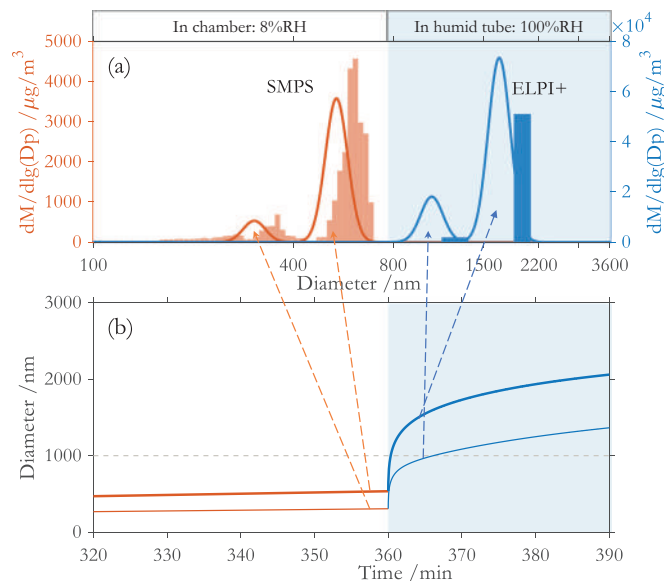


**Fig. 8.** Model predicted particle size evolution and size distributions in the chamber and the humid tube (in solid lines), in which the measured size distributions from SMPS (red) and ELPI+ are represented in bars (blue). (For interpretation of the references to color in this figure legend, the reader is referred to the web version of this article.)

that intermediate- and semi-volatile organics are the primary contributors to the increased SOA in the humid tube.

Since the haze is usually associated with different NO<sub>x</sub> conditions, we further did an additional chamber experiment with moderate (NO = 1.0 ppb, NO<sub>2</sub> = 15.6 ppb) NO<sub>x</sub> level. Other conditions were the same as the low NO<sub>x</sub> experiments. The results show that there were more species due to the formation of N-containing products than low NO<sub>x</sub> conditions. SOA mass in the humid tube was increased by 65 % compared to the dry channel (Fig. S2). This value is slightly smaller than the low NO<sub>x</sub> system (67 %). In addition, similar to the low NO<sub>x</sub> experiment, the increased SOA (moderate NO<sub>x</sub>) was mainly contributed by monomeric gas-phase products with  $m/z < 210$ . Thus, it shows the influence of organic vapors on the interaction between aerosol and fog can be applied to low and moderate NO<sub>x</sub> conditions.

### 3.3. Explosive growth of SOA under humid conditions

The evolution of SOA size distribution in the chamber and the humid tube was simulated by CSVA (Fig. 8). The results show bimodal size distributions in both dry conditions (in the chamber) and super humid conditions (in the humid tube), which agree well with the experimental observation (Fig. 8a). The predicted mean diameters are generally smaller than the measured ones. Under the dry condition, the model-predicted mean diameter for the larger peak is 13 % less than the measured data (43 % smaller for the smaller peak); under the super humid condition, the model-predicted mean diameters for the bimodal are about 16 % smaller than the measured values. We found that the model predicted particle number concentration ( $5.67 \times 10^3/\text{cm}^3$ ) is 17 % larger than the experimental data ( $4.84 \times 10^3/\text{cm}^3$ ), which is the primary reason for the difference in diameters between the model and experiment. In addition, both experimental and model results show that the difference between the smaller and larger peaks was enlarged in the humid tube, which can be explained by Köhler theory that water vapor is prone to partition into larger particles.

To reveal the microphysical process of SOA particles in the humid tube, we plotted the Köhler curves considering the co-condensation of all gas-phase products (Fig. 9). The Köhler curves of SOA exhibit similar trends to that from NaCl-PTLQOH in a closed system (Fig. 1). The Köhler curves are very close to the curves determined by Raoult's law. Thus, the solute effect mainly governs the hygroscopic growth of SOA particles. Due to the co-

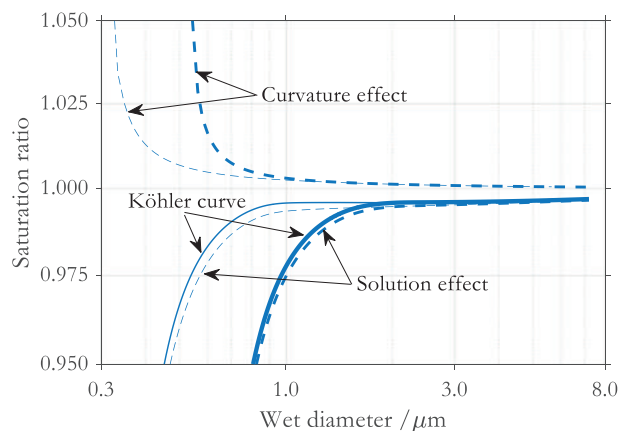


**Fig. 9.** Equilibrium saturation ratio for SOA particles with co-condensation of monomeric products from toluene oxidation in the humid tube at 20 °C. The thin curves are for the first smaller peak mode and the bold curves for the larger peak mode.

condensation of gas-phase products, the first maximum saturation ratio is only 0.996 for the smaller mode (0.995 for the larger mode). If an aerosol particle has been activated, its saturation ratio will decrease with the diameter. However, with the depletion of organics from the gas phase due to partition, condensation becomes weak, and the curves re-increased slightly with particle diameters. It shows that the particles were not fully activated; however, they could grow up to 7  $\mu\text{m}$  droplets with co-condensation of organic vapors.

The kinetic interaction between water and organics is studied during hygroscopic growth and evaporation. The evolutions of LWC and SOA mass concentrations are simulated in different situations (Fig. 10). After 6 h of reaction, the chamber supplies the initial sample air with RH = 8 % at time point of 360 min. The humid tube provides a humid environment for hygroscopic growth or activation with RH = 100 % (360–390 min), and the dry tube serves as an evaporation condition with RH = 8 % (390–420 min). The maximum LWC is only 3.4  $\mu\text{g}/\text{m}^3$  in the chamber at 8 % RH with a corresponding GF value close to 1.0, which is in accord with the measured GF for SOA particles (Varutbangkul et al., 2006). LWC rapidly increases to 3  $\text{mg}/\text{m}^3$  within the first minute when the chamber air is introduced into the humid tube. Meanwhile, SOA's mass concentrations also increase by 47 % from 436 to 643  $\mu\text{g}/\text{m}^3$  after 30 min of humidification. The dash lines in Fig. 10 present the LWC and SOA without considering the condensation of organics during the hygroscopic growth process. If redistribution of organic vapors is not considered, LWC is only proportional to the SOA mass concentration, and SOA is independent of LWC. This is a typical treatment in most chemical transport models, where LWC is mainly calculated based

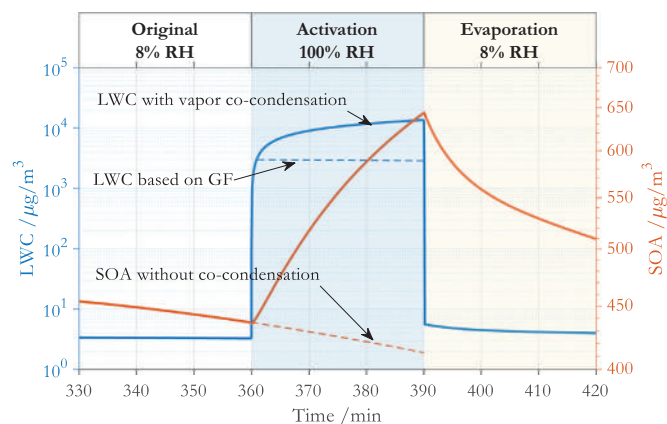


**Fig. 10.** Model simulated evolution of LWC and SOA mass concentrations during activation and evaporation.

on inorganic salts (Ervens, 2015). Based on GF and SOA mass concentration, the maximum LWC can only reach 2.9  $\text{mg}/\text{m}^3$ . Instead, LWC keeps increasing due to the addition of solutes from the gas phase, reaching 13  $\text{mg}/\text{m}^3$  within 30 min. When the humid air is further introduced into the dry tube for evaporation, LWC is quickly dropped from 13  $\text{mg}/\text{m}^3$  to 5.6  $\mu\text{g}/\text{m}^3$  within 0.6 s. Due to the low vapor pressure of organics, the organics' evaporation is much slower than water. There is still 510  $\mu\text{g}/\text{m}^3$  SOA left after 30 min of evaporation. Our results demonstrate that the co-condensation of water vapor can significantly enhance SOA formation.

Previous laboratory studies indicate that (acid-catalyzed) heterogeneous reactions under high RH might play an important role in SOA formation from aromatic compounds (Jang et al., 2002; Zhou et al., 2011). On the other hand, high RH is more likely to induce relatively lower aerosol acidity, thus reducing the enhancement of SOA formation by acidity (Liang et al., 2019). The acid-catalyzed particle-phase reactions have been considered in the CSVA model, in which the dimers of SOA were mainly formed through particle-phase reactions, which differ from monomers of SOA from the gas phase. To investigate the possibility of heterogeneous reactions under high RH, we further simulated the evolution of dimers in the super humid tube (100 %). It shows that due to the activation of SOA particles, the explosive increase of LWC significantly diluted the liquid concentration of monomers, leading to the decomposing of dimers to corresponding monomers (95 % of SOA contributed by monomers at 100 %RH). After the evaporation at 10 % RH, the abundance of monomers reduced to 85 %. This value is close to the experimental data that monomers contribute 80 % of SOA. Our results agree well with previous studies that high RH has a positive effect on SOA formation from aromatics (Zhou et al., 2011; Jia and Xu, 2014, 2018); meanwhile, the relative contributions of dimers were significantly reduced during the fog period.

#### 3.4. Coupled effect of temperature and humidity on SOA formation and activation

The partitioning equilibrium constant  $K_{pT}$  has an exponential growth with decreasing temperature based on Eq. (1). Taking PTLQOH as an example, when the temperature decreases from 300 to 233 K, the  $K_{pT}$  can exponentially increase from 0.028 to 8731  $\text{m}^3/\mu\text{g}$  (Fig. S3). Hence, the influence of organic vapors' co-condensing can be significantly enlarged with decreasing temperatures. To examine the combined effects of RH and T, we further simulated the formation of toluene SOA with a wide range of temperatures. To make the simulations closer to ambient conditions, the initial concentrations of toluene, NO and  $\text{NO}_2$  were correspondingly set to be 100, 60 and 20 ppb. The effective light intensity of  $\text{NO}_2$  was set to be 0.4  $\text{min}^{-1}$ . Since most of the condensed water remains liquid at a temperature down to  $-37.5$  °C in deep convective clouds (Rosenfeld and Woodley, 2000), we assumed that the particles are in a liquid state as  $T > -40$  °C for simplicity. To obtain the maxima of SOA with 8 h of irradiation, we performed 1600 model simulations under different RH and T conditions. The LWC and SOA isopleths are plotted as a function of RH and T (Fig. 11). When RH is below 85 %, the ridgeline divides the area into two regimes. The ridgeline identifies the maximum LWC or SOA that can be achieved at a given temperature, allowing RH to vary. It shows that the formation of SOA is more sensitive to RH in the left part of the ridgeline than in the right regime. Increasing temperature can reduce gas to particle partition while enhancing the reaction rate constants. The net result of such an opposite effect is the presence of a ridgeline. Both LWC and SOA maxima show a steep increase when RH and T fall into the triangle region of  $\text{RH} > 85$  % and  $T < 20$  °C (red color). As discussed above, when soluble organic gases are dissolved in aqueous droplets, the equilibrium saturation ratio of the droplets is lowered. Since the  $K_{pT}$  values increase exponentially with decreasing T, the Köhler curve maximum can be significantly depressed at  $<100$  % RH at a lower temperature. If the concentration of organic vapors is high, aerosols can be easily activated into the fog or cloud droplets. The accumulation of LWC further leads to the explosive growth of SOA. Our discovery can well explain the explosive growth of SOA during serious haze events, which are associated with high relative humidity and low temperatures.

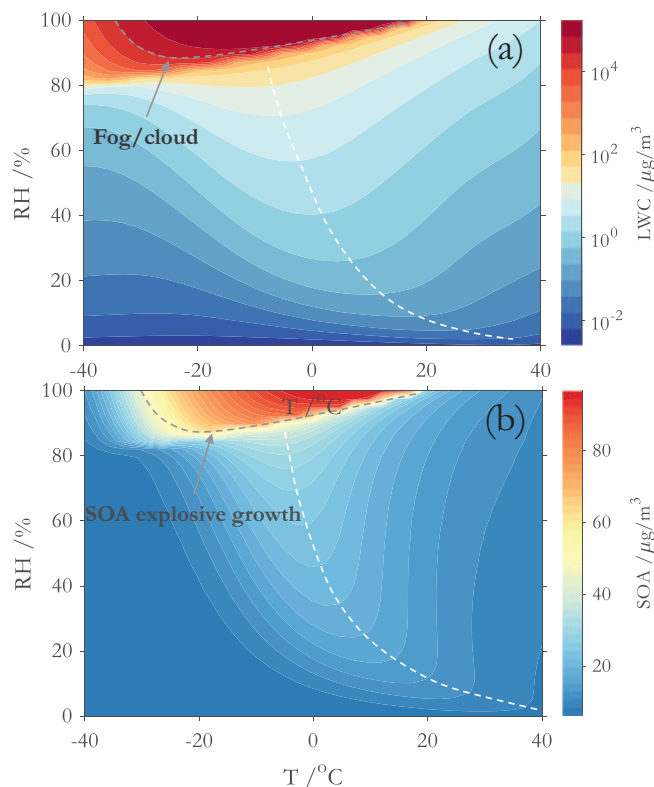


**Fig. 11.** Coupled effect of temperature and relative humidity on LWC (a) and SOA (b) from toluene. The white dashed line represents the ridgeline, and the gray dashed line represents the explosive growth region.

### 3.5. E-CSVA modeling

To constrain the relative importance of aerosol-fog interactions on SOA formation in ambient conditions, we further simulated aerosol evolution with E-CSVA. The typical cycle of a haze episode lasts 4 to 7 days in Beijing (Guo et al., 2014; Sun et al., 2016; Wang et al., 2021). It starts with a dry and clean condition and then undergoes the influence of southeast surface winds accompanied by large amounts of water vapor for the first 3 to 5 days. The aerosols accumulate during the southeast wind prevailing period. On the last day, the air is cleaned by dry and clean northwest winds. Boundary mixed layer height, MH, is a crucial factor controlling the species' evolution in the boundary layer. MH has a diurnal variation on clear days; however, during the heavy haze period, MH variation becomes rather weak due to temperature inversion, a so-called stagnant weather condition. The typical meteorological conditions were set based on these facts. We simulated two scenarios: (1) the atmosphere was under stagnant conditions with a fixed MH at 600 m (Case 1); and (2) MH had a diurnal variation in the range of 300 to 1100 m (Case 2).

Fig. 12 shows evolutions of meteorological parameters and chemical species during a five-day haze episode in Case 1. The gas species (e.g., toluene and  $\text{NO}_x$ ) have reached stable cycles after the 2nd day; hence, all conditions excluding RH are the same between the 2nd and 4th day. The RH gradually increases with the southeast wind, beginning from 34.0 % to 55.0 % (1st day), 92.7 % (2nd day), 94.2 % (3rd day) and 94.5 % (4th day) at the sunrise time. On the 5th day, the dry and clean northwest wind decreases the RH to 42.2 %. The dilution due to the rise of MH will disappear under stagnant conditions, which can lead to the accumulation of particle mass concentrations. To rule out the PM stack due to the fixed MH, we slightly reduced the RH to ensure that no fog occurred during the haze episode (Fig. S4). It shows that SOA only increases by  $8.7 \mu\text{g}/\text{m}^3$  during one day at RH of 88.1 % to 89.8 %.

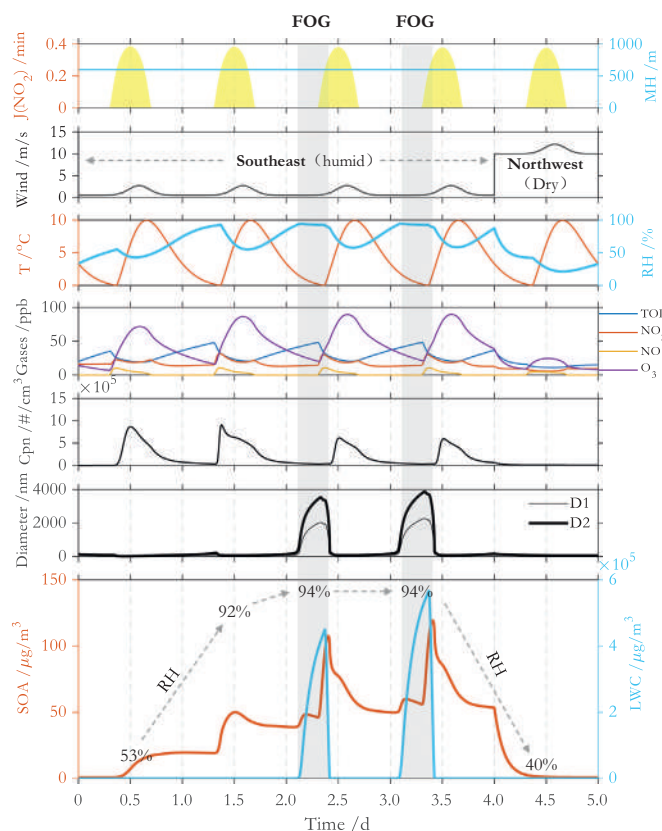


**Fig. 12.** Time series of meteorological parameters and chemical species without diurnal variation of mixing layer height.

On the first day of Case 1, the maximum SOA is  $19.6 \mu\text{g}/\text{m}^3$  as RH gradually increases from 34.0 to 74.0 %. When RH rises from 55 % (1st day) to 92.7 % (2nd day), the corresponding maximum SOA reaches  $49.4 \mu\text{g}/\text{m}^3$ . To deduct the contribution from the accumulated part due to stagnant weather conditions, we also simulate a case with similar conditions as Case 1 except for MH, in which MH changes in the range of 300 to 1100 m (Case 1'). The difference in maximum SOA mass between the two cases is due to the stagnant weather conditions. After deducting the contribution from the accumulated part due to stagnant weather conditions, the SOA increases by a factor of two under high RH conditions, which is consistent with ambient observations (An et al., 2019; Peng et al., 2021). The positive effect of RH on SOA formation can be explained by the elevation of the gas-particle partitioning equilibrium constant due to the presence of aerosol water, as supported by laboratory experiments (Jia and Xu, 2014, 2018; Zhou et al., 2011) and the kinetical simulations (Jia and Xu, 2021).

Due to the continual addition of solutes from gas-phase SVOCs, the haze particles can be activated into fog droplets at RH below 100 %. The fog occurs when RH arrives at 94.2 % (94.5 %) in the early morning of the 3rd day (4th day). It shows that the RH curve reaches a steady state during the foggy period, a sign of fog formation. During the foggy period on the 3rd day, LWC quickly increases from tens of  $\mu\text{g}/\text{m}^3$  to  $0.45 \text{ g}/\text{m}^3$ , and the average diameter of particles in the first peak rises from 0.09 to  $2.0 \mu\text{m}$  (0.17 to  $3.5 \mu\text{m}$  for the 2nd peak). Accompanying fog formation before sunrise, SOA increases by 27 % ( $37.7$  to  $47.5 \mu\text{g}/\text{m}^3$ ) from SVOCs partitioning. After the sunrise, SOA increases to a maximum of  $106.8 \mu\text{g}/\text{m}^3$  with the additional supply of SVOCs from photochemistry. Compared to the non-foggy condition on the 2nd day, the corresponding SOA mass increases by 125 %. After removing the accumulation due to the fixed MH, the SOA increases by 107 % under the foggy environment.

When MH variation is included (Case2 in Fig. S5), the fogs also occur on the 3rd and 4th days, but fog time is reduced from 6.7 to 3.4 h compared to

Case 1. Meanwhile, LWC is decreased to 0.07 g/m<sup>3</sup>. When RH increases from 91.9% (on the 2nd-day haze) to 93.6% (3rd-day fog), the corresponding SOA increases by 79% (from 40.7 to 73.0 µg/m<sup>3</sup>). It shows that the stagnant weather conditions can strengthen the fog, which, in turn, enhances the SOA formation. Thus, the phase transformation of water can profoundly influence SOA formation, while organic aerosol explosive formation is closely linked with fog microphysics.

In ambient conditions, inorganic salt aerosols also make a significant contribution. Based on partitioning theory (Steinfeld and Pandis, 2016), the presence of background salt aerosols could enhance the formation of SOA. To consider the effect of salt aerosol, we included NH<sub>4</sub>NO<sub>3</sub> in E-CSVA, where the reaction between NH<sub>3</sub> and HNO<sub>3</sub> forms NH<sub>4</sub>NO<sub>3</sub>. HNO<sub>3</sub> was formed from the toluene-NO<sub>x</sub> system. In this study, we assumed that NH<sub>3</sub> was so sufficient that particle phase HNO<sub>3</sub> existed in NH<sub>4</sub>NO<sub>3</sub>. After including the inorganic salt aerosol, we found that the maximum increases of SOA were about 19% during non-fog conditions and 2% during fog conditions. Since most water-soluble organics are already in the particle phase, the presence of background salt has little effect on SOA formation during the fog period (Fig. S6).

It should be noted that fog formation may reduce the UV radiation, which could influence SOA formation. Clouds usually have a reducing effect on UV radiation. Still, many works report an enhancement effect of clouds on UV radiation, as surmised by Calbó et al. (2005). The specific impact of surface fog on UV radiation is unknown. Anyway, we tested the reducing effect of fog on UV radiation. If light intensity was reduced by 50% during the fog period, SOA peak concentrations on the 2nd and 3rd days were only decreased by 9%. In addition, most of the duration of fog events happens before sunrise. Hence, we did not consider the reducing effect of fog on UV radiation.

### 3.6. Atmospheric implications

The increased organic aerosol during the haze-fog periods was generally attributed to the aqueous reactions. However, aqueous reactions in the particle phase mainly involve functionalization and fragmentation. Functionalization can yield high molecular weight species, whereas fragmentation can generate more-volatile species and cause the reduction of SOA formation (Jimenez et al., 2009; Lim et al., 2010). Many studies have confirmed that fragmentation reactions were key steps in oxygenated organic aerosol-forming and evolving processes (Isaacman-VanWertz et al., 2018; Kroll et al., 2009). Additionally, the rate of explosive increases is so quick that aqueous chemistry cannot explain the process thoroughly. Our results demonstrate that the physical processes are responsible for the explosive formation of SOA. It shows that haze is closely intertwined with fog, and that the presence of SVOC can reduce the critical supersaturation ratio, leading to fog or cloud droplets with RH below or near 100%. The condensation of water can, in turn, drive SOA's explosive growth by partitioning SVOCs. It has been supported by the field observations that SOA significantly increased under fog conditions (Eck et al., 2020; Zhang et al., 2020). A recent field study from Gkatzelis et al. (2021) pointed out that uptake of water-soluble small aldehydes and acids by aerosol water may drive organic particulate pollution in Beijing. In addition, the low temperature can further amplify such an effect, as shown in Fig. 11, which can provide a reasonable explanation for winter haze pollution in severe cold climate regions, e.g., Harbin (Cheng et al., 2022, 2021) and Urumqi (Liu et al., 2017). Due to the complexity of SOA, it may be difficult for the field study to distinguish the contribution of SOA that formed from the co-condensation of water-soluble organics and water or particle-phase reactions. Our chamber experiments and model results show that the aqueous-phase processes in the field observations combined the co-condensation process and particle-phase reactions. Benefiting from the most advanced mass spectrometer and an online coupled dynamic model, we can investigate the interaction between aerosol and fog with the influence of organic vapors. Our results show that E-CSVA performs well in analyzing SOA formation in field studies.

## 4. Conclusions

In this study, we investigated the interaction between SOA and fog with the influence of organic vapors based on a high-resolution mass spectrometer and an online coupled dynamic model (CSVA). Our results showed that haze was closely intertwined with fog and that the presence of water-soluble organic vapors can reduce the critical supersaturation ratio, leading to fog or cloud droplets with relative humidity below or near 100%. The condensation of water can, in turn, drive SOA's explosive growth by partitioning of water-soluble organics. In particular, we demonstrated that low temperatures could dramatically amplify water-soluble organic vapor influence on SOA explosive formation and CCN activation. Previous attempts to predict liquid water content in field studies were generally based on the thermodynamics models (e.g., ISORROPIA or E-AIM) using the inorganic aerosol composition, and the role of organic aerosol was overlooked. In contrast, our results show that the phase transformation of water can profoundly influence SOA formation, and organic aerosol explosive formation is closely linked with fog microphysics.

### CRedit authorship contribution statement

**Long Jia:** Conceptualization, Data curation, Formal analysis, Funding acquisition, Investigation, Project administration, Methodology, Software, Visualization, Writing – original draft. **YongFu Xu:** Funding acquisition, Investigation, Project administration, Resources, Supervision, Validation, Visualization, Writing – review & editing. **MinZheng Duan:** Methodology, Writing – review & editing.

### Data availability

Data will be made available on request.

### Declaration of competing interest

The authors declare that they have no known competing financial interests or personal relationships that could have appeared to influence the work reported in this paper.

### Acknowledgments

This work was supported by the Beijing Natural Science Foundation (8212039), the National Natural Science Foundation of China (Nos. 41875166, 41875163 and 42175125) and the National Key Scientific and Technological Infrastructure project “Earth System Science Numerical Simulator Facility” (EarthLab).

### Appendix A. Supplementary data

Supplementary data to this article can be found online at <https://doi.org/10.1016/j.scitotenv.2022.161338>.

## References

- An, Z., Huang, R.J., Zhang, R., Tie, X., Li, G., Cao, J., Zhou, W., Shi, Z., Han, Y., Gu, Z., Ji, Y., 2019. Severe haze in northern China: a synergy of anthropogenic emissions and atmospheric processes. *Proc. Natl. Acad. Sci. U. S. A.* 116, 8657–8666. <https://doi.org/10.1073/pnas.1900125116>.
- Calbó, J., Pagès, D., González, J.A., 2005. Empirical studies of cloud effects on UV radiation: a review. *Rev. Geophys.* 43, 1–28. <https://doi.org/10.1029/2004RG000155>.
- Cheng, Y., Yu, Q.Q., Liu, J.M., Cao, X.B., Zhong, Y.J., Du, Z.Y., Liang, L.L., Geng, G.N., Ma, W.L., Qi, H., Zhang, Q., He, K.Bin, 2021. Dramatic changes in Harbin aerosol during 2018–2020: the roles of open burning policy and secondary aerosol formation. *Atmos. Chem. Phys.* 21, 15199–15211. <https://doi.org/10.5194/acp-21-15199-2021>.
- Cheng, Y., Cao, X., Liu, J., Zhu, S., Wang, S., Yu, Q., Zhang, H., Zhang, Q., He, K., 2022. Overestimated role of sulfate in haze formation over Chinese megacities due to improper simulation of heterogeneous reactions. *Environ. Chem. Lett.* <https://doi.org/10.1007/s10311-022-01464-3>.

- Davies, J.F., Zuend, A., Wilson, K.R., 2019. Technical note: the role of evolving surface tension in the formation of cloud droplets. *Atmos. Chem. Phys.* 19, 2933–2946. <https://doi.org/10.5194/acp-19-2933-2019>.
- Derwent, R.G., Jenkin, M.E., Utembe, S.R., Shallcross, D.E., Murrells, T.P., Passant, N.R., 2010. Secondary organic aerosol formation from a large number of reactive man-made organic compounds. *Sci. Total Environ.* 408, 3374–3381. <https://doi.org/10.1016/j.scitotenv.2010.04.013>.
- Donahue, N.M., Epstein, S.A., Pandis, S.N., Robinson, A.L., 2011. A two-dimensional volatility basis set: 1. Organic-aerosol mixing thermodynamics. *Atmos. Chem. Phys.* 11, 3303–3318. <https://doi.org/10.5194/acp-11-3303-2011>.
- Eck, T.F., Holben, B.N., Kim, J., Beyersdorf, A.J., Choi, M., Lee, S., Koo, J.H., Giles, D.M., Schafer, J.S., Sinyuk, A., Peterson, D.A., Reid, J.S., Arola, A., Slutsker, I., Smirnov, A., Sorokin, M., Kraft, J., Crawford, J.H., Anderson, B.E., Thornhill, K.L., Diskin, G., Kim, S.W., Park, S., 2020. Influence of cloud, fog, and high relative humidity during pollution transport events in South Korea: aerosol properties and PM<sub>2.5</sub> variability. *Atmos. Environ.* 232, 117530. <https://doi.org/10.1016/j.atmosenv.2020.117530>.
- Epstein, S.A., Riipinen, I., Donahue, N.M., 2010. A semiempirical correlation between enthalpy of vaporization and saturation concentration for organic aerosol. *Environ. Sci. Technol.* 44, 743–748. <https://doi.org/10.1021/es902497z>.
- Ervens, B., 2015. Modeling the processing of aerosol and trace gases in clouds and fog. *Chem. Rev.* 115, 4157–4198. <https://doi.org/10.1021/cr5005887>.
- Fu, G.Q., Xu, W.Y., Yang, R.F., Li, J.B., Zhao, C.S., 2014. The distribution and trends of fog and haze in the North China Plain over the past 30 years. *Atmos. Chem. Phys.* 14, 11949–11958. <https://doi.org/10.5194/acp-14-11949-2014>.
- Gkatzelis, G.I., Papanastasiou, D.K., Karydis, V.A., Hohaus, T., Liu, Ying, Schmitt, S.H., Schlag, P., Fuchs, H., Novelli, A., Chen, Q., Cheng, X., Broch, S., Dong, H., Holland, F., Li, X., Liu, Yuhuan, Ma, X., Reimer, D., Rohrer, F., Shao, M., Tan, Z., Taraborrelli, D., Tillmann, R., Wang, H., Wang, Y., Wu, Y., Wu, Z., Zeng, L., Zheng, J., Hu, M., Lu, K., Hofzumahaus, A., Zhang, Y., Wahner, A., Kiendler-Scharr, A., 2021. Uptake of water-soluble gas-phase oxidation products drives organic particulate pollution in Beijing. *Geophys. Res. Lett.* 48. <https://doi.org/10.1029/2020GL091351>.
- Göttsche, F.M., Olesen, F.S., 2001. Modelling of diurnal cycles of brightness temperature extracted from meteosat data. *Remote Sens. Environ.* 76, 337–348. [https://doi.org/10.1016/S0034-4257\(00\)00214-5](https://doi.org/10.1016/S0034-4257(00)00214-5).
- Goulden, G., Crooks, M., Connolly, P., 2018. Uncertainty in aerosol hygroscopicity resulting from semi-volatile organic compounds. *Atmos. Chem. Phys.* 18, 275–287. <https://doi.org/10.5194/acp-18-275-2018>.
- Guo, S., Hu, M., Zamora, M.L., Peng, J., Shang, D., Zheng, J., Du, Z., Wu, Z., Shao, M., Zeng, L., Molina, M.J., Zhang, R., 2014. Elucidating severe urban haze formation in China. *Proc. Natl. Acad. Sci.* 111, 17373–17378. <https://doi.org/10.1073/pnas.1419604111>.
- Guo, H., Ling, Z.H., Cheng, H.R., Simpson, I.J., Lyu, X.P., Wang, X.M., Shao, M., Lu, H.X., Ayoko, G., Zhang, Y.L., Saunders, S.M., Lam, S.H.M., Wang, J.L., Blake, D.R., 2017. Tropospheric volatile organic compounds in China. *Sci. Total Environ.* 574, 1021–1043. <https://doi.org/10.1016/j.scitotenv.2016.09.116>.
- Gysel, M., Weingartner, E., Baltensperger, U., 2002. Hygroscopicity of aerosol particles at low temperatures. 2. Theoretical and experimental hygroscopic properties of laboratory generated aerosols. *Environ. Sci. Technol.* 36, 63–68. <https://doi.org/10.1021/es010055g>.
- Hegg, D.A., 2000. Impact of gas-phase HNO<sub>3</sub> and NH<sub>3</sub> on microphysical processes in atmospheric clouds. *Geophys. Res. Lett.* 27, 2201–2204. <https://doi.org/10.1029/1999GL011252>.
- Hu, D., Topping, D., McFiggans, G., 2018. Measured particle water uptake enhanced by co-condensing vapours. *Atmos. Chem. Phys.* 18, 14925–14937. <https://doi.org/10.5194/acp-18-14925-2018>.
- IPCC, 2013. Working group I contribution to the IPCC fifth Assessment Report (AR5). *Climate change 2013: the physical science basis*. Geneva, Switzerland.
- Isaacman-VanWertz, G., Massoli, P., O'Brien, R., Lim, C., Franklin, J.P., Moss, J.A., Hunter, J.F., Nowak, J.B., Canagaratna, M.R., Misztal, P.K., Arata, C., Roscioli, J.R., Herndon, S.T., Onasch, T.B., Lambe, A.T., Jayne, J.T., Su, L., Knopf, D.A., Goldstein, A.H., Worsnop, D.R., Kroll, J.H., 2018. Chemical evolution of atmospheric organic carbon over multiple generations of oxidation. *Nat. Chem.*, 1–7. <https://doi.org/10.1038/s41557-018-0002-2>.
- Jang, M., Czoschke, N.M., Lee, S., Kamens, R.M., 2002. Heterogeneous atmospheric aerosol production by acid-catalyzed particle-phase reactions. *Science* 298, 814–817. <https://doi.org/10.1126/science.1075798>.
- Jia, L., Xu, Y., 2014. Effects of relative humidity on ozone and secondary organic aerosol formation from the photooxidation of benzene and ethylbenzene. *Aerosol Sci. Technol.* 48, 1–12. <https://doi.org/10.1080/02786826.2013.847269>.
- Jia, L., Xu, Y., 2018. Different roles of water in secondary organic aerosol formation from toluene and isoprene. *Atmos. Chem. Phys.* 18, 8137–8154. <https://doi.org/10.5194/acp-18-8137-2018>.
- Jia, L., Xu, Y., 2020. The role of functional groups in the understanding of secondary organic aerosol formation mechanism from  $\alpha$ -pinene. *Sci. Total Environ.* 738, 139831. <https://doi.org/10.1016/j.scitotenv.2020.139831>.
- Jia, L., Xu, Y., 2021. A core-shell box model for simulating viscosity dependent secondary organic aerosol (CSVA) and its application. *Sci. Total Environ.* 789, 147954. <https://doi.org/10.1016/j.scitotenv.2021.147954>.
- Jia, X., Quan, J., Zheng, Z., Liu, X., Liu, Q., He, H., Liu, Y., 2019. Impacts of anthropogenic aerosols on fog in North China Plain. *J. Geophys. Res. Atmos.* 124, 252–265. <https://doi.org/10.1029/2018JD029437>.
- Jimenez, J.L., Canagaratna, M.R., Donahue, N.M., Prevot, A.S.H., Zhang, Q., Kroll, J.H., DeCarlo, P.F., Allan, J.D., Coe, H., Ng, N.L., Aiken, A.C., Docherty, K.S., Ulbrich, I.M., Grieshop, A.P., Robinson, A.L., Duplissy, J., Smith, J.D., Wilson, K.R., Lanz, V.A., Hueglin, C., Sun, Y.L., Tian, J., Laaksonen, A., Raatikainen, T., Rautiainen, J., Vaattovaara, P., Ehn, M., Kulmala, M., Tomlinson, J.M., Collins, D.R., Cubison, M.J., Dunlea, E.J., Huffman, J.A., Onasch, T.B., Alfarra, M.R., Williams, P.I., Bower, K., Kondo, Y., Schneider, J., Drewnick, F., Borrmann, S., Weimer, S., Demerjian, K., Salcedo, D., Cottrell, L., Griffin, R., Takami, A., Miyoshi, T., Hatakeyama, S., Shimono, A., Sun, J.Y., Zhang, Y.M., Dzepina, K., Kimmel, J.R., Sueper, D., Jayne, J.T., Herndon, S.C., Trimborn, A.M., Williams, L.R., Wood, E.C., Middlebrook, A.M., Kolb, C.E., Baltensperger, U., Worsnop, D.R., 2009. Evolution of organic aerosols in the atmosphere. *Science* 326, 1525–1529. <https://doi.org/10.1126/science.1180353>.
- Kelly, F.J., Fussler, J.C., 2015. Air pollution and public health: emerging hazards and improved understanding of risk. *Environ. Health Perspect.* 123, 631–649. <https://doi.org/10.1007/s10653-015-9720-1>.
- Köhler, H., 1936. The nucleus in and the growth of hygroscopic droplets. *Trans. Faraday Soc.* 32, 1152–1161. <https://doi.org/10.1039/TF9363201152>.
- Kokkola, H., Romakkaniemi, S., Laaksonen, A., 2003. Köhler theory for a polydisperse droplet population in the presence of a soluble trace gas, and an application to stratospheric STS droplet growth. *Atmos. Chem. Phys.* 3, 2139–2146. <https://doi.org/10.5194/acp-3-2139-2003>.
- Kroll, J.H., Smith, J.D., Che, D.L., Kessler, S.H., Worsnop, D.R., Wilson, K.R., 2009. Measurement of fragmentation and functionalization pathways in the heterogeneous oxidation of oxidized organic aerosol. *Phys. Chem. Chem. Phys.* 11, 8005. <https://doi.org/10.1039/b905289e>.
- Kulmala, M., Laaksonen, A., Korhonen, P., Vesala, T., Ahonen, T., Barrett, J.C., 1993. The effect of atmospheric nitric acid vapor on cloud condensation nucleus activation. *J. Geophys. Res.* 98. <https://doi.org/10.1029/93jd02070>.
- Kulmala, M., Laaksonen, A., Charlson, R.J., Korhonen, P., 1997. Clouds without supersaturation. *Nature* 388, 336–337. <https://doi.org/10.1038/41000>.
- Laaksonen, A., Korhonen, P., Kulmala, M., Charlson, R.J., 1998. Modification of the Köhler equation to include soluble trace gases and slightly soluble substances. *J. Atmos. Sci.* 55, 853–862. [https://doi.org/10.1175/1520-0469\(1998\)055<0853:MOTKHE>2.0.CO;2](https://doi.org/10.1175/1520-0469(1998)055<0853:MOTKHE>2.0.CO;2).
- Lamkaddam, H., Dommen, J., Ranjithkumar, A., Gordon, H., Wehrle, G., Krechmer, J., Majluf, F., Salionov, D., Schmale, J., Bjelić, S., Carslaw, K.S., El Haddad, I., Baltensperger, U., 2021. Large contribution to secondary organic aerosol from isoprene cloud chemistry. *Sci. Adv.* 7. <https://doi.org/10.1126/sciadv.abe2952>.
- Li, Q., Su, G., Li, C., Liu, P., Zhao, X., Zhang, C., Sun, X., Mu, Y., Wu, M., Wang, Q., Sun, B., 2020. An investigation into the role of VOCs in SOA and ozone production in Beijing, China. *Sci. Total Environ.* 720, 137536. <https://doi.org/10.1016/j.scitotenv.2020.137536>.
- Li, G., Su, H., Ma, N., Tao, J., Kuang, Y., Wang, Q., Hong, J., Zhang, Y., Kuhn, U., Zhang, S., Pan, X., Lu, N., Tang, M., Zheng, G., Wang, Z., Gao, Y., Cheng, P., Xu, W., Zhou, G., Zhao, C., Yuan, B., Shao, M., Ding, A., Zhang, Q., Fu, P., Sun, Y., Poschl, U., Cheng, Y., 2021. Multiphase chemistry experiment in fogs and aerosols in the North China Plain (McFAN): integrated analysis and intensive winter campaign 2018. *Faraday Discuss.* 226, 207–222. <https://doi.org/10.1039/d0fd00099j>.
- Liang, L., Engling, G., Cheng, Y., Zhang, X., Sun, J., Xu, W., Liu, C., Zhang, G., Xu, H., Liu, X., Ma, Q., 2019. Influence of high relative humidity on secondary organic carbon: observations at a background site in East China. *J. Meteorol. Res.* 33, 905–913. <https://doi.org/10.1007/s13351-019-8202-2>.
- Lim, Y.B., Tan, Y., Perri, M.J., Seitzinger, S.P., Turpin, B.J., 2010. Aqueous chemistry and its role in secondary organic aerosol (SOA) formation. *Atmos. Chem. Phys.* 10, 10521–10539. <https://doi.org/10.5194/acp-10-10521-2010>.
- Liu, T., Zhuang, G., Huang, K., Lin, J., Wang, Q., Deng, C., Fu, J.S., 2017. A typical formation mechanism of heavy haze-fog induced by coal combustion in an inland city in north-western China. *Aerosol Air Qual. Res.* 17, 98–107. <https://doi.org/10.4209/aaqr.2016.04.0143>.
- Liu, P., Song, M., Zhao, T., Gunthe, S.S., Ham, S., He, Y., Qin, Y.M., Gong, Z., Amorim, J.C., Bertram, A.K., Martin, S.T., 2018. Resolving the mechanisms of hygroscopic growth and cloud condensation nuclei activity for organic particulate matter. *Nat. Commun.* 9. <https://doi.org/10.1038/s41467-018-06622-2>.
- Liu, Z., Hu, B., Ji, D., Cheng, M., Gao, W., Shi, S., Xie, Y., Yang, S., Gao, M., Fu, H., Chen, J., Wang, Y., 2019. Characteristics of fine particle explosive growth events in Beijing, China: seasonal variation, chemical evolution pattern and formation mechanism. *Sci. Total Environ.* 687, 1073–1086. <https://doi.org/10.1016/j.scitotenv.2019.06.068>.
- Liu, Q., Wang, Z., Yu, W., B. Gui, Liu, J., Nie, H., Hao, Chen, D., Hua, G., Gultepe, I., 2021. Microphysics of fog bursting in polluted urban air. *Atmos. Environ.* 253, 118357. <https://doi.org/10.1016/j.atmosenv.2021.118357>.
- Lowe, S.J., Partridge, D.G., Davies, J.F., Wilson, K.R., Topping, D., Riipinen, I., 2019. Key drivers of cloud response to surface-active organics. *Nat. Commun.* 10. <https://doi.org/10.1038/s41467-019-12982-0>.
- Luo, H., Jia, L., Wan, Q., An, T., Wang, Y., 2019. Role of liquid water in the formation of O<sub>3</sub> and SOA particles from 1,2,3-trimethylbenzene. *Atmos. Environ.* 217, 116955. <https://doi.org/10.1016/j.atmosenv.2019.116955>.
- Peng, J., Hu, M., Shang, D., Wu, Z., Du, Z., Tan, T., Wang, Y., Zhang, F., Zhang, R., 2021. Explosive secondary aerosol formation during severe haze in the North China Plain. *Environ. Sci. Technol.* 55, 2189–2207. <https://doi.org/10.1021/acs.est.0c07204>.
- Quan, J., Zhang, Q., He, H., Liu, J., Huang, M., Jin, H., 2011. Analysis of the formation of fog and haze in North China Plain (NCP). *Atmos. Chem. Phys.* 11, 8205–8214. <https://doi.org/10.5194/acp-11-8205-2011>.
- Rosenfeld, D., Woodley, W.L., 2000. Deep convective clouds with sustained supercooled liquid water down to -37.5 °C. *Nature* 405, 440–442. <https://doi.org/10.1038/35013030>.
- Ruehl, C.R., Davies, J.F., Wilson, K.R., 2016. An interfacial mechanism for cloud droplet formation on organic aerosols. *Science* 351, 1447–1450. <https://doi.org/10.1126/science.1254889>.
- Sheng, J., Zhao, D., Ding, D., Li, X., Huang, M., Gao, Y., Quan, J., Zhang, Q., 2018. Characterizing the level, photochemical reactivity, emission, and source contribution of the volatile organic compounds based on PTR-TOF-MS during winter haze period in Beijing, China. *Atmos. Res.* 212, 54–63. <https://doi.org/10.1016/j.atmosres.2018.05.005>.
- Sorjamaa, R., Svenningsson, B., Raatikainen, T., Henning, S., Bilde, M., Laaksonen, A., 2004. The role of surfactants in Köhler theory reconsidered. *Atmos. Chem. Phys.* 4, 2107–2117. <https://doi.org/10.5194/acp-4-2107-2004>.

- Steinfeld, J.I., Pandis, S.N., 2016. *Atmospheric Chemistry and Physics: From Air Pollution to Climate Change* 3rd Edition. 3rd ed. John Wiley.
- Sulaymon, I.D., Zhang, Yuanxun, Hopke, P.K., Hu, J., Zhang, Yang, Li, L., Mei, X., Gong, K., Shi, Z., Zhao, B., Zhao, F., 2021. Persistent high PM<sub>2.5</sub> pollution driven by unfavorable meteorological conditions during the COVID-19 lockdown period in the Beijing-Tianjin-Hebei region, China. *Environ. Res.* 198, 111186. <https://doi.org/10.1016/j.envres.2021.111186>.
- Sun, Y., Jiang, Q., Xu, Y., Ma, Y., Zhang, Y., Liu, X., Li, W., Wang, F., Li, J., Wang, P., Li, Z., 2016. Aerosol characterization over the North China Plain: haze life cycle and biomass burning impacts in summer. *J. Geophys. Res. Atmos.* 121, 2508–2521. <https://doi.org/10.1002/2015JD024261>.
- Tang, G., Zhang, Jinqiang, Zhu, X., Song, T., Münkler, C., Hu, B., Schäfer, K., Liu, Z., Zhang, Junke, Wang, L., Xin, J., Suppan, P., Wang, Y., 2016. Mixing layer height and its implications for air pollution over Beijing, China. *Atmos. Chem. Phys.* 16, 2459–2475. <https://doi.org/10.5194/acp-16-2459-2016>.
- Topping, D.O., McFiggans, G.B., Coe, H., 2005. A curved multi-component aerosol hygroscopicity model framework: part 2 - including organic compounds. *Atmos. Chem. Phys.* 5, 1223–1242. <https://doi.org/10.5194/acp-5-1223-2005>.
- Topping, D., Connolly, P., McFiggans, G., 2013. Cloud droplet number enhanced by co-condensation of organic vapours. *Nat. Geosci.* 6, 443–446. <https://doi.org/10.1038/ngeo1809>.
- Varutbangkul, V., Brechtel, F.J., Bahreini, R., Ng, N.L., Keywood, M.D., Kroll, J.H., Flagan, R.C., Seinfeld, J.H., Lee, A., Goldstein, A.H., 2006. Hygroscopicity of secondary organic aerosols formed by oxidation of cycloalkenes, monoterpenes, sesquiterpenes, and related compounds. *Atmos. Chem. Phys.* 6, 2367–2388. <https://doi.org/10.5194/acp-6-2367-2006>.
- Wang, Y., Luo, H., Jia, L., Ge, S., 2016. Effect of particle water on ozone and secondary organic aerosol formation from benzene-NO<sub>2</sub>-NaCl irradiations. *Atmos. Environ.* 140, 386–394. <https://doi.org/10.1016/j.atmosenv.2016.06.022>.
- Wang, H., Peng, Y., Zhang, X., Liu, H., Zhang, M., Che, H., Cheng, Y., Zheng, Y., 2018. Contributions to the explosive growth of PM<sub>2.5</sub> mass due to aerosol-radiation feedback and decrease in turbulent diffusion during a red alert heavy haze in Beijing-Tianjin-Hebei, China. *Atmos. Chem. Phys.* 18, 17717–17733. <https://doi.org/10.5194/acp-18-17717-2018>.
- Wang, J., Li, J., Ye, J., Zhao, J., Wu, Y., Hu, J., Liu, D., Nie, D., Shen, F., Huang, X., Huang, D.D., Ji, D., Sun, X., Xu, W., Guo, J., Song, S., Qin, Y., Liu, P., Turner, J.R., Lee, H.C., Hwang, S., Liao, H., Martin, S.T., Zhang, Q., Chen, M., Sun, Y., Ge, X., Jacob, D.J., 2020. Fast sulfate formation from oxidation of SO<sub>2</sub> by NO<sub>2</sub> and HONO observed in Beijing haze. *Nat. Commun.* 11, 2844. <https://doi.org/10.1038/s41467-020-16683-x>.
- Wang, J., Ye, J., Zhang, Q., Zhao, J., Wu, Y., Li, J., Liu, D., Li, W., Zhang, Y., Wu, C., Xie, C., Qin, Y., Lei, Y., Huang, X., Guo, J., Liu, P., Fu, P., Li, Y., Lee, H.C., Choi, H., Zhang, J., Liao, H., Chen, M., Sun, Y., Ge, X., Martin, S.T., Jacob, D.J., 2021. Aqueous production of secondary organic aerosol from fossil-fuel emissions in winter Beijing haze. *Proc. Natl. Acad. Sci. U. S. A.* 118, 1–6. <https://doi.org/10.1073/pnas.2022179118>.
- Wang, Yonghong, Clusius, P., Yan, C., Dällenbach, K., Yin, R., Wang, M., He, X.C., Chu, B., Lu, Y., Dada, L., Kangasluoma, J., Rantala, P., Deng, C., Lin, Z., Wang, W., Yao, L., Fan, X., Du, W., Cai, J., Heikkinen, L., Tham, Y.J., Zha, Q., Ling, Z., Junninen, H., Petäjä, T., Ge, M., Wang, Yuesi, He, H., Worsnop, D.R., Kerminen, V.M., Bianchi, F., Wang, L., Jiang, J., Liu, Y., Boy, M., Ehn, M., Donahue, N.M., Kulmala, M., 2022. Molecular composition of oxygenated organic molecules and their contributions to organic aerosol in Beijing. *Environ. Sci. Technol.* 56, 770–778. <https://doi.org/10.1021/acs.est.1c05191>.
- Wei, W., Li, Y., Wang, Y., Cheng, S., Wang, L., 2018. Characteristics of VOCs during haze and non-haze days in Beijing, China: concentration, chemical degradation and regional transport impact. *Atmos. Environ.* 194, 134–145. <https://doi.org/10.1016/j.atmosenv.2018.09.037>.
- Yang, Y., Ge, B., Chen, X., Yang, W., Wang, Zhongjie, Chen, H., Xu, D., Wang, J., Tan, Q., Wang, Zifa, 2021. Impact of water vapor content on visibility: fog-haze conversion and its implications to pollution control. *Atmos. Res.* 256, 105565. <https://doi.org/10.1016/j.atmosres.2021.105565>.
- Yu, J., Wang, Y., Liu, M., 2021. Mechanisms of an extreme fog and haze event in the megacities of central and eastern China. *Meteorol. Atmos. Phys.* 133, 123–139. <https://doi.org/10.1007/s00703-020-00737-2>.
- Yu, S., Jia, L., Xu, Y., Pan, Y., 2022. Formation of extremely low-volatility organic compounds from styrene ozonolysis: implication for nucleation. *Chemosphere* 305, 135459. <https://doi.org/10.1016/j.chemosphere.2022.135459>.
- Zhang, J., Lance, S., Marto, J., Sun, Y., Ninneman, M., Crandall, B.A., Wang, J., Zhang, Q., Schwab, J.J., 2020. Evolution of aerosol under moist and fog conditions in a rural forest environment: insights from high-resolution aerosol mass spectrometry. *Geophys. Res. Lett.* 47. <https://doi.org/10.1029/2020GL089714>.
- Zhong, J., Zhang, X., Dong, Y., Wang, Y., Liu, C., Wang, J., Zhang, Y., Che, H., 2018. Feedback effects of boundary-layer meteorological factors on cumulative explosive growth of PM<sub>2.5</sub> during winter heavy pollution episodes in Beijing from 2013 to 2016. *Atmos. Chem. Phys.* 18, 247–258. <https://doi.org/10.5194/acp-18-247-2018>.
- Zhou, Y., Zhang, H., Parikh, H.M., Chen, E.H., Rattanavaraha, W., Rosen, E.P., Wang, W., Kamens, R.M., 2011. Secondary organic aerosol formation from xylenes and mixtures of toluene and xylenes in an atmospheric urban hydrocarbon mixture: water and particle seed effects (II). *Atmos. Environ.* 45, 3882–3890. <https://doi.org/10.1016/j.atmosenv.2010.12.048>.
- Ziemann, P.J., Atkinson, R., 2012. Kinetics, products, and mechanisms of secondary organic aerosol formation. *Chem. Soc. Rev.* 41, 6582. <https://doi.org/10.1039/c2cs35122f>.